Postprint

Impedance Spectroscopy Modeling of Nickel–Molybdenum Alloys on Porous and Flat Substrates for Applications in Water Splitting

İlknur Bayrak Pehlivan*, Miguel A. Coyotzi, Zhen Qiu,

Gunnar A. Niklasson, Tomas Edvinsson**

Department of Engineering Sciences, The Ångström Laboratory, Uppsala University, P.O. Box 534, 75121 Uppsala, Sweden

Abstract

Hydrogen production by splitting water using electrocatalysts powered by renewable energy from solar or wind plants is one promising alternative to produce a carbon–free and sustainable fuel. Earth–abundant and non–precious metals are here of interest as a replacement for scarce and expensive platinum group catalysts. Ni–Mo is a promising alternative to Pt but the type of substrate could ultimately affect both the initial growth conditions as well as the final charge transfer in the system as a whole with resistive junctions formed in the heterojunction interface. In this study, we investigated the effect of different substrates on the hydrogen evolution reaction (HER) of Ni–Mo electrocatalysts. Ni–Mo catalysts (30 at. % Ni, 70 at. % Mo) were sputtered on various substrates with different porosity and conductivity. There was no apparent morphological difference at the

surface of the catalytic films sputtered on the different substrates, and the substrates were classified from microporous to flat. The electrochemical characterization was carried out with linear sweep voltammetry (LSV) and electrochemical impedance spectroscopy (EIS) in the frequency range 0.7 Hz–100 kHz. LSV measurements were carried out at DC potentials between 200 and –400 mV vs. the reversible hydrogen electrode (RHE) in 1 M NaOH encompassing the HER. The lowest overpotentials for HER were obtained for films on nickel foam at all current densities (–157 mV vs. RHE @ 10 mA cm^{-2}), and the overpotentials increased in the order of nickel foil, carbon cloth, fluorine doped tin oxide and indium tin oxide glass, respectively. EIS data were fitted with two equivalent circuit models and compared for different DC potentials and different substrate morphologies and conductivities. By critical evaluation of the data from the models, the influence of the substrates on the reaction kinetics was seen in the high– and low–frequency region. In the high–frequency region, a strong substrate dependence was seen and interpreted with a Schottky–type barrier, which can be rationalized as being due to a potential barrier in the material heterojunctions or a resistive substrate–film oxide/hydroxide. The results highlight the importance of substrates, the total charge transfer properties in electrocatalysis, the relevance of different circuit components in EIS as well as underpin the necessity to incorporate high conductivity, chemically inert and work function matched substrate–catalysts in the catalyst system.

*ilknur.bayrak_pehlivan@angstrom.uu.se

**tomas.edvinsson@angstrom.uu.se

1. Introduction

The late and equitable raise in the standard of living around the world, together with increases in population, leads to a strong increase in the demand for energy. The high present and forecasted consumption together with ensuing environmental problems using fossil fuels or nuclear power have dramatically increased the need for using more environmentally sustainable energy sources .[1–3] Renewable energy such as solar and wind energy can be converted to electrical energy, and their market share is rapidly increasing. However, the considerable variability of the power delivered from renewable energy sources, the intermittency, necessitates the development of energy storage. [4–7] Here, hydrogen is one promising alternative to store electrical energy from renewable sources[8] and represents the highest stored energy content per weight. The hydrogen can be produced by wind-electrolysis or from solar energy via both a photoelectrochemical and a photovoltaic–electrolysis approach[9,10] for later use as a carbon–free fuel or for producing electricity on demand in stationary or mobile applications via fuel cells.[11] As mentioned above, the need to solve the intermittency problem with wind and solar energy, has markedly increased the international interest in renewable hydrogen production. The interest and ongoing activities are also paralleled by projects in using less intermittent energy sources such as hydropower for producing green–hydrogen as a feedstock chemical for industry.
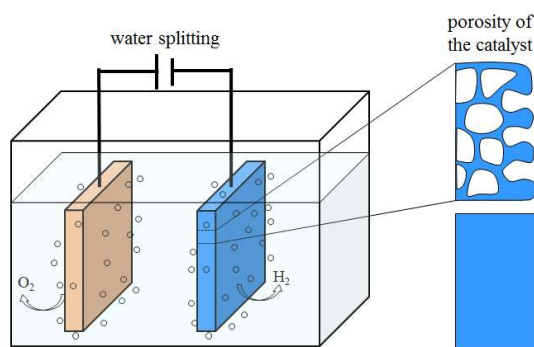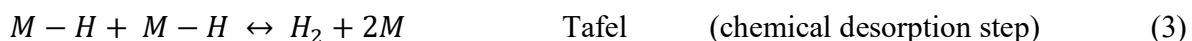
Figure 1. Schematic picture of an electrolyzer where hydrogen is produced via water splitting and different porosity of the catalyst-substrate system.

Hydrogen can be produced from either reformation of fossil fuels or electrolysis of a hydrogen–containing chemical. Here, water splitting[12–16] from water–based electrolytes using renewable energy sources represents a nearly carbon–neutral energy cycle. Figure 1 shows a schematic picture of water splitting occurring in an electrolyzer consisting of two catalytic electrodes. On the right side of the figure, catalysts with porous or flat morphologies are illustrated.

Water splitting consists of two half–reactions which are the oxygen evolution reaction on the surface of the anodic catalyst and the hydrogen evolution reaction (HER) on the cathodic catalyst. HER in alkaline solutions can be considered to occur in three different steps or as their combination.[17, 18]

$$M + H_2O + e^- \leftrightarrow M - H + OH^- \qquad \text{Volmer} \qquad \text{(electrochemical adsorption step)} \quad (1)$$

$$M - H + H_2O + e^- \leftrightarrow H_2 + OH^- + M \quad \text{Heyrovsky} \quad \text{(electrochemical desorption step)} \quad (2)$$

$$M - H + M - H \leftrightarrow H_2 + 2M \qquad \text{Tafel} \qquad \text{(chemical desorption step)} \qquad (3)$$

where M represents the active sites on the electrocatalyst such as Ni and Mo.

It is known that Pt is the most efficient catalyst for electrolysis for HER,[19] but development of catalysts based on earth–abundant and non-precious alternatives are of great importance for large scale applications. Transition metal-based electrocatalysts are here widely employed for HER in alkaline media. Various material classes have been investigated to improve and understand the catalytic activities such as synthesis metals, alloys, oxides, hydroxides, sulfides, selenides, tellurides, nitrides, phosphides, carbides, and borides.[20-22] Improvement in the catalytic activities can be achieved using strategies such as component regulation, defect engineering, doping, phase

engineering, facet engineering, interface engineering, enriching active sites through nanosizing, designing dimensional architectures (0–3D), porous structuring, and enhancing conductivity with the assistance of highly conductive substrates.[22-24] Ni–Mo alloys are one of the best non–precious electrocatalysts which can be a promising alternative to Pt for the HER,[25–27] in competition with Fe–Ni layered double hydroxides that recently was shown to transform to oxyhydroxides under strongly alkaline conditions exhibiting a more effective catalysis for HER than Pt.[28]

The efficiency of a catalyst depends on the electrochemical properties of the system and thus on the catalyst–electrolyte interface, the porosity of the catalyst, reaction kinetics, electrolyte resistivity, and charge transport in the catalyst. Electrochemical impedance spectroscopy (EIS) is an excellent technique to investigate and understand the mechanisms that influence electrocatalytic properties.[29–31] The impedance due to a reaction with adsorbed intermediates has been derived theoretically[32] and applied to the study of the HER.[33] The impedance response may show one or two semicircles in the Z–plane, depending on the rate constants of the reaction steps.[34, 35] In principle, it is possible to obtain the parameters of the HER reaction directly by fitting to impedance spectra.[33, 36] However, the reaction response is frequently complicated by overlap with other phenomena such as diffusion processes, charge transport in an interlayer on the electrodes and geometrical effects due to porosity and roughness. In such cases, it is appropriate to fit impedance data to equivalent circuit models, in order to disentangle different phenomena.

In this work, we study the effects of substrates with different porosity and conductivity for a Ni–Mo catalyst on the HER in the case of water splitting. Structural and electrochemical properties of the catalysts, as well as their performance on the different substrates, were examined. The results were interpreted by using two common equivalent circuit models for the impedance response of the catalysts.

2. Experimental

2.1. Sample preparation

Ni–Mo films were deposited on different substrates, i.e., Ni foam, Ni foil, carbon cloth (C–cloth), indium tin oxide (ITO) coated glass and fluorine doped tin oxide (FTO) coated glass. The films were prepared by reactive DC magnetron co–sputtering using a Balzers UTT 400 unit. The targets were two 5 cm diameter metallic Ni (99.99% purity, Plasmaterials) and Mo (99.99% purity, Plasmaterials) discs. The target to substrate distance was 13 cm. Pre–sputtering was performed for 5 min to clean the surface of the targets. Depositions were done at 30 mTorr pressure, with 50 ml/min Ar flow, and using powers of 80 and 180 W for Ni and Mo, respectively. Similar conditions have been used in previous studies.[27] The substrate holder was rotated at 3 rpm to improve the homogeneity of the films. The film thickness determined by a Veeco Dektak 150 surface profilometry instrument was 160±10 nm.

2.2. Characterization techniques

Elemental composition of the films was determined with Rutherford backscattering spectrometry (RBS) using 2 MeV $^4He^{2+}$ ions backscattered at an angle of 170°. The RBS data were fitted to a model of the film–substrate system by use of the SIMNRA simulation program for a ~1000 nm thick Ni–Mo film on FTO.[37] The Ni–Mo proportion was found to be 30 at.% Ni and 70 at.% Mo (± 0.1 at.%).

Structural characterization of as-deposited Ni–Mo films was performed with X-ray diffraction (XRD) using a grazing-incidence Siemens D5000 diffractometer using $CuK_{\alpha 1}$ radiation (1.5406 Å) in a range of 2θ from 10 ° to 80 ° with steps of 0.02 °. The results were compared with the XRD patterns of pristine substrates and Ni–Mo on Si substrate. As seen from the XRD patterns in Fig.

S1, there was no significant diffraction peaks other than those assigned to the substrates, which indicated that the Ni–Mo films had an amorphous structure, similar to a previous study.[27]

Surface morphology of the films was analyzed by a Zeiss 1550 scanning electron microscopy (SEM) instrument equipped with an In–lens detector to obtain secondary electron images and operated at 5 kV accelerating voltage. Energy–dispersive X–ray spectroscopy (EDS) was performed at 20 kV accelerating voltage. X–ray mapping and elemental analysis were analyzed by Aztec software.

The electrochemical measurements were performed with a three–electrode configuration at room temperature. An Ag/AgCl electrode (E_0 = 0.199 V at 25 °C) and a Pt wire were used as reference and counter electrode, respectively. The electrolyte was 1M NaOH (pH=14). All potentials measured in this work were measured with respect to the Ag/AgCl reference electrode and transformed to the reversible hydrogen electrode (RHE) potential at pH=14 via $E_{RHE} = E_0 + E_{Ag/AgCl} + 0.059$ pH (and thus adding +1.03 V to the measured potential). Linear sweep voltammetry (LSV) measurements were performed using a CH Instrument model 760C workstation between 200 and –400 mV vs. RHE with a scan rate of 1 mV s^{-1}. EIS measurements were performed using a Zahner Zennium electrochemical workstation. The frequency was swept over 47 points between 0.7 Hz and 100 kHz. The measurements were done using a 10 mV amplitude AC potential at various applied DC potentials between 200 and –400 mV vs. RHE. Analysis of the impedance data was done using the ZView software (Scribner Associates, Inc).[38]

3. Results and discussions

SEM was employed to study the morphology of the Ni–Mo films coated on Ni foam, C–cloth, ITO and Ni foil. Figure 2 shows SEM images of the films deposited on the porous and flat

substrates on the micrometer and nanometer scale where one sees that there is a uniform coverage on the flat and rough substrates and fairly uniform on the porous substrates. The catalytic films showed similar homogeneity on the nanometer scale (Figure 2 c, d and Figure S2 (a–d)) with cracks separated by 30–50 nm. Uniform elemental coverage of the Ni and Mo on the substrates was established by EDS (Figure S2 (e–f)).
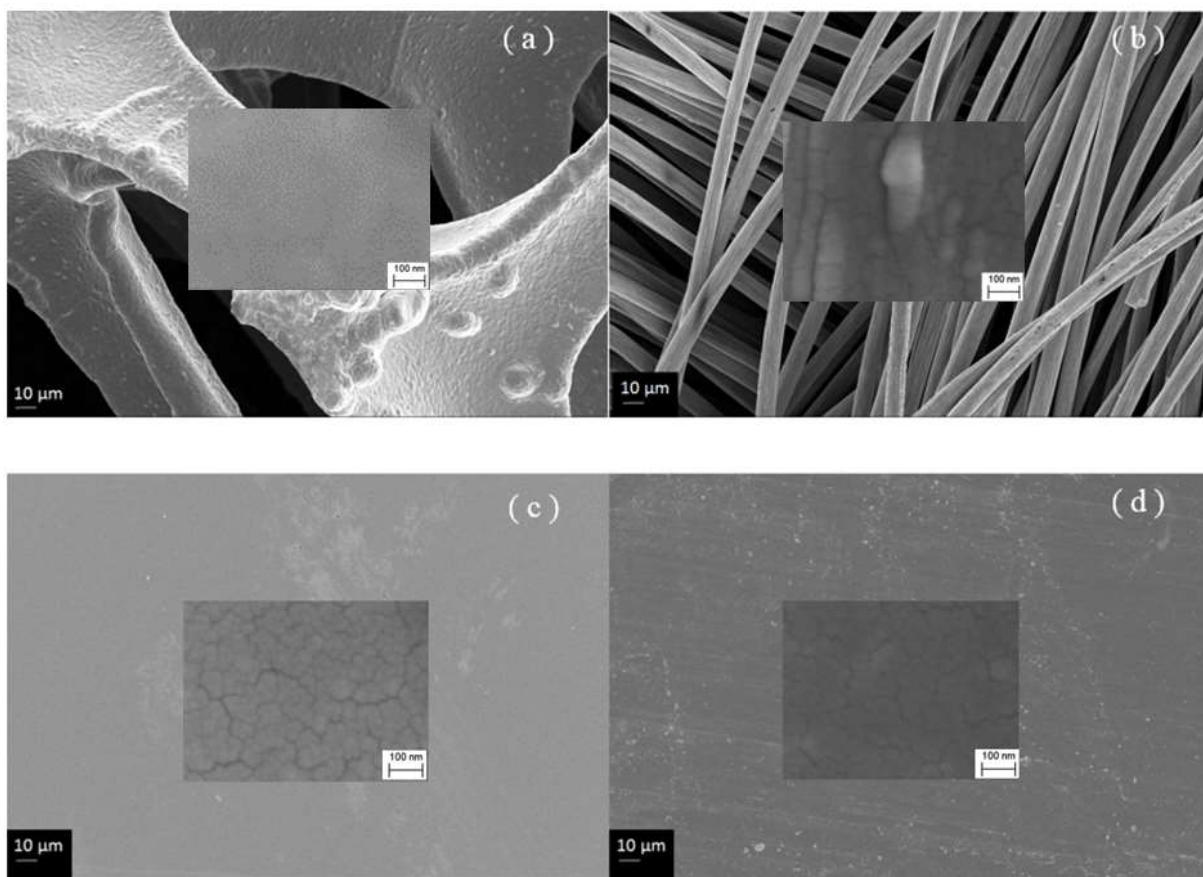

Figure 2. SEM images of the Ni–Mo films on Ni foam (a), C–cloth (b), ITO (c), and Ni foil (d) The scale bars on the black background and white background (inset) in the micrographs are 10 μm and 100 nm, respectively.

Figure 3 (a) shows LSV of the Ni–Mo films coated on different substrates in the potential region relevant for the HER. It was seen that the HER rate was highest for the film coated on Ni foam,

followed by the ones coated on Ni foil, C–cloth, FTO and ITO, respectively. Specifically, the current density of 10 mA cm^{-2}, seen in the embedded image in Fig. 3 (a), was reached at –157, –177 and –209 mV vs. RHE for the Ni–Mo films coated on Ni foam, Ni foil, and C–cloth. However, the films on ITO and FTO could not reach 10 mA cm^{-2} current density in the studied potential range. This is not only reflecting that the lower surface area for the Ni–Mo catalyst film on flat substrates limits high currents, but the differences in–between the flat substrates also indicate that both high surface area and beneficial contact and conductivity between the substrate and catalytic material are essential for the catalyst system. Figure 3 (b) shows the Tafel plots in the low overpotential region for Ni–Mo films on different substrates. The results for the films on different substrates showed a similar behaviour and the Tafel slopes were above 60 mV/decade. This shows that the Heyrovsky step was rate–determining for the Ni–Mo films on Ni substrates, while the high Tafel slopes for films on FTO and ITO may indicate a rate–determining Volmer step, although the Heyrovsky step cannot be ignored.[39] Hence the low reactivity of films on FTO and ITO may be due to a slower adsorption kinetics in these cases.
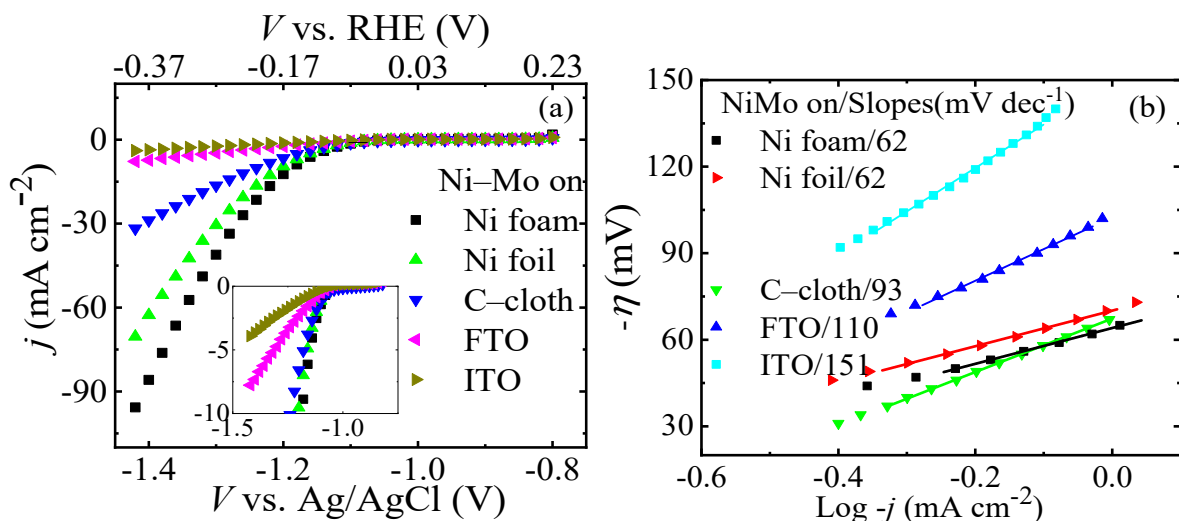
Figure 3. Current density (j) versus applied potential (V) (a) and Tafel plot (b) of overpotential as a function of logarithm of current density for Ni–Mo films on different substrates in 1M NaOH measured by LSV with 1 mV s^{-1} scan rate.

EIS measurements were performed on the Ni–Mo films coated on different substrates. The experimental data were fitted with two different models, here denoted *EqCrt1* and *EqCrt2*, shown in Fig. 4 (a) and (b), respectively. The *EqCrt1* model consists of a series connection of a resistance ($R_{s,1}$), an inductance (L_1), a parallel connection of a high frequency resistance ($R_{hf,1}$) and a high frequency constant phase element ($CPE_{hf,1}$), and a parallel connection of a low frequency resistance ($R_{lf,1}$) and a low frequency constant phase element ($CPE_{lf,1}$). The *EqCrt2* model consists of a series connection of a resistance ($R_{s,2}$), an inductance (L_2), a parallel connection of a high frequency constant phase element ($CPE_{hf,2}$) and a high frequency resistance ($R_{hf,2}$), which has a series connection with a parallel connected low frequency resistance ($R_{lf,2}$) and low frequency constant phase element ($CPE_{lf,2}$). The impedance function of a constant phase element can be written as

$$Z_{CPE}^* = [T(i\omega)^P]^{-1} \tag{4}$$

where ω is angular frequency, T is a parameter related to the electrode capacitance, and P is the constant phase exponent. These two models are the most common equivalent circuit models used for HER in the case of capacitive behavior in the low–frequency region.[35–38] However, physical interpretations of the models are different. The elements R_s and L are apparently due to the electrolyte and electrical connections, but we now consider the interpretation of the remaining circuit elements. In the first model, the high frequency part is related to the surface geometry, and the low–frequency part is associated with the reaction kinetics while the second model can be derived directly from the reaction kinetics,[32, 33] together with the double layer surface effects which

can be obtained from $CPE_{hf,2}$. In this latter model, $R_{hf,2}$ should be the reaction charge transfer resistance, while $CPE_{lf,2}$ and $R_{lf,2}$ would be associated with the response due to changes in the coverage of adsorbed species. For perfect capacitive behavior (that is, when $P = 1$ in Eq. 4), the circuits are essentially equivalent, while the possibility to numerically distinguish the two models depends on the deviation of the constant phase elements exponent from unity and the accuracy of the experimental data.
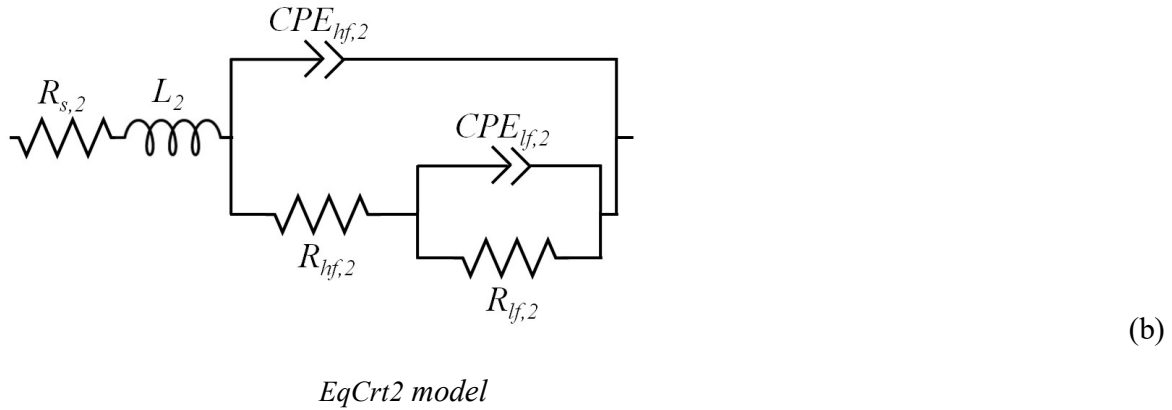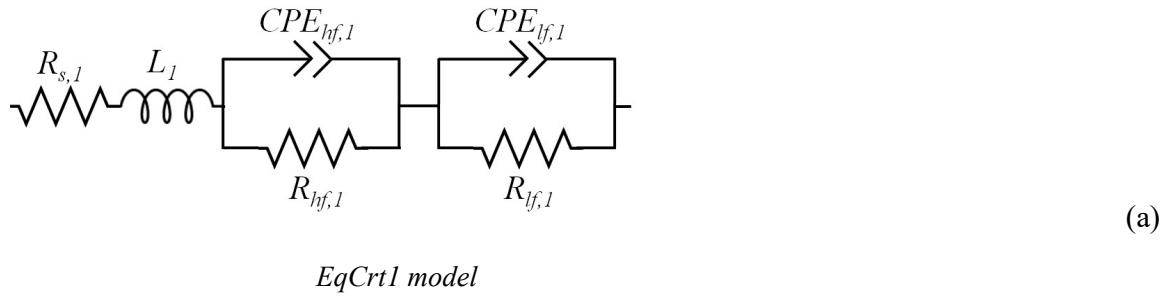

(a)

EqCrt1 model

(b)

EqCrt2 model

Figure 4. Equivalent circuit models abbreviated *EqCrt1* (a) and *EqCrt2* (b) used for fitting data of Ni–Mo catalysts.

The Nyquist plots of the experimental data at different DC potentials are shown together with the *EqCrt1* and *EqCrt2* circuit model fits in Fig. 5 (a) and (b) for the films on Ni foam and in Fig. 5 (c) and (d) for the films on ITO, respectively. Similar plots for the films coated on Ni foil, C–cloth, and FTO can be found in Fig. S3–S5. It is seen that all the spectra exhibit two arcs in the

measured frequency range, which are in many cases overlapping. It should be noted that the highest frequencies are at the left–hand side of the Nyquist plots and that frequencies decrease as one follows the curves towards the right. The lowest frequencies represent the highest impedance. For the films on Ni foam, the two arcs were almost overlapping, and the impedance response was dominated by the second arc in the lower frequency range which exhibited the higher impedance values. The high–frequency range with the underlying second arc is shown in more detail in the inset in Fig. 5 (b). For Ni–Mo on ITO, the high–frequency arc was large enough to be clearly distinguished from the low–frequency behavior. The high–frequency arc was larger than the second arc at DC potentials below –200 mV vs. RHE. As seen in Fig. S3–S5, the spectral behavior of the films on Ni foil and C–cloth were similar to the spectra of the films on the Ni foam while the spectra of the films on FTO resemble those of the films on ITO. For all different substrates, the absolute impedance in the low–frequency range decreased considerably with increasing negative DC potential.
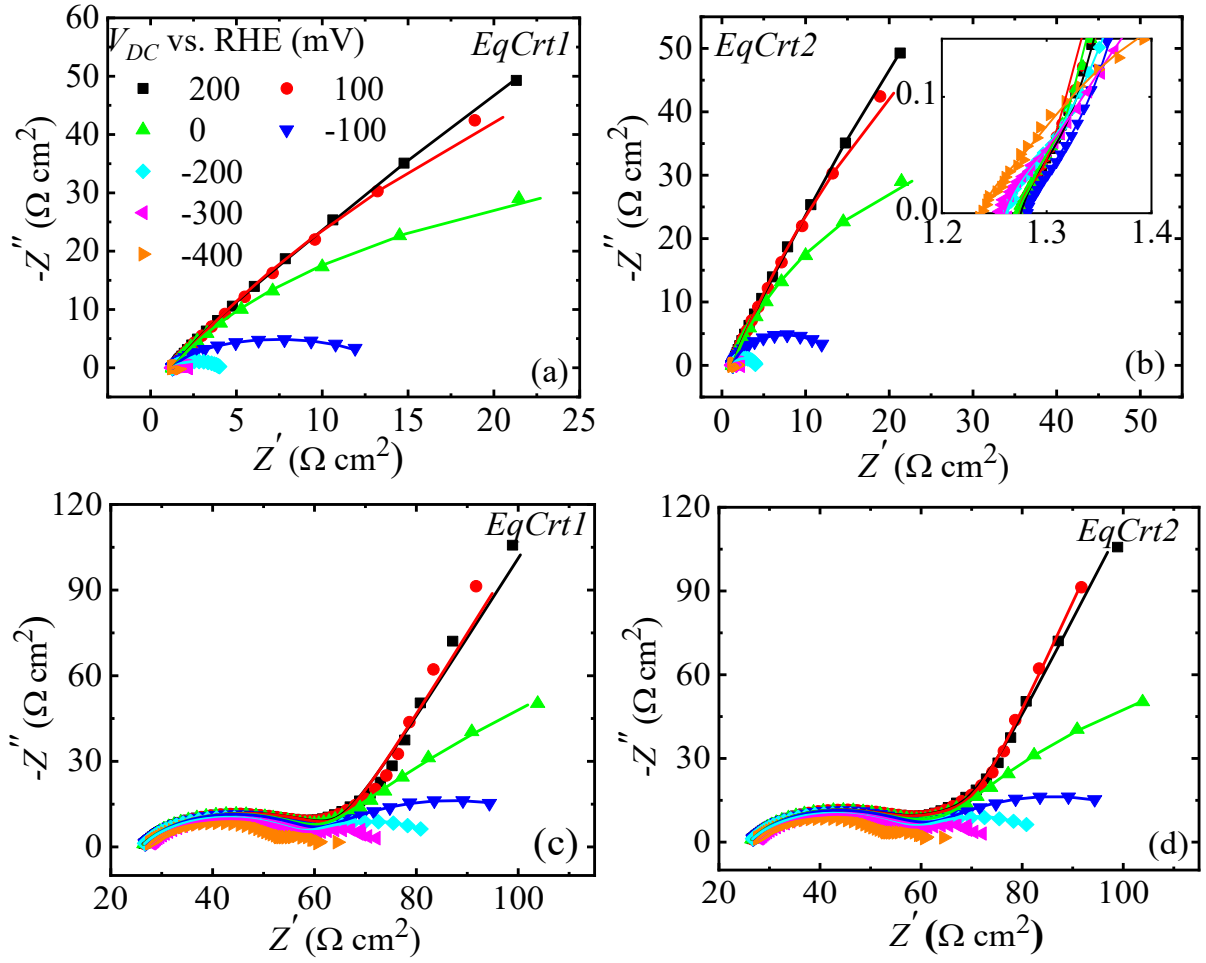
Figure 5. Nyquist plots for Ni–Mo catalysts on Ni foam (a) and (b) and on ITO (c) and (d) at different DC potentials vs. RHE. Experimental data are shown by symbols and impedance fits to *EqCrt1* (a, c) and *EqCrt2* (b, d) are shown by lines. Legend in (a) are valid for (b), (c) and (d) as well.

As seen in Fig. 5, the *EqCrt1* and *EqCrt2* models generally show good agreement with the experimental data with slight deviations at positive potentials outside the HER region. The sum of square deviations of the fits for the *EqCrt1* and *EqCrt2* models with respect to the experimental data for the Ni–Mo films sputtered on various substrates, which is proportional to the average percentage error between the original and calculated data, was always less than 0.08, and mostly

below 0.02. In some cases, the C–cloth data were difficult to fit, resulting in uncertain parameter values due to covariance of parameters.

The parameters of the fitted *EqCrt1* and *EqCrt2* circuit models were plotted versus potential as a function of the applied DC potential for the Ni–Mo films on different substrates. An inductive element (L) was needed for some of the data (Fig. S6). Additional measurements, not presented here, showed that the presence of L was dependent on the experimental conditions such as the arrangement of the setup, the cables, etc. This element was desired in some cases to take into account trivial lead inductances; hence there will not be further analysis of it in this study.

The R_s values versus potential obtained from the *EqCrt1* and *EqCrt2* are shown in Fig. S7 (a) and (b), respectively, for Ni–Mo films on different substrates. It was seen that similar values were obtained from both models and they were not significantly potential dependent but increased in the order of Ni foam, Ni foil, C–cloth, FTO and ITO. The R_{hf} values from the fitting of EIS data of Ni–Mo films on different substrates using *EqCrt1* and *EqCrt2* are shown in Fig. 6 (a) and S8 (a), respectively. The values obtained were not significantly different at different potentials in the HER region, taking into account the higher fitting uncertainty for the C–cloth data. However, there was a noticeable dependence of R_{hf} on the kind of substrate. The general trend was an increase in the values of R_{hf} in the order of Ni foam, Ni foil, C–cloth, FTO and ITO.
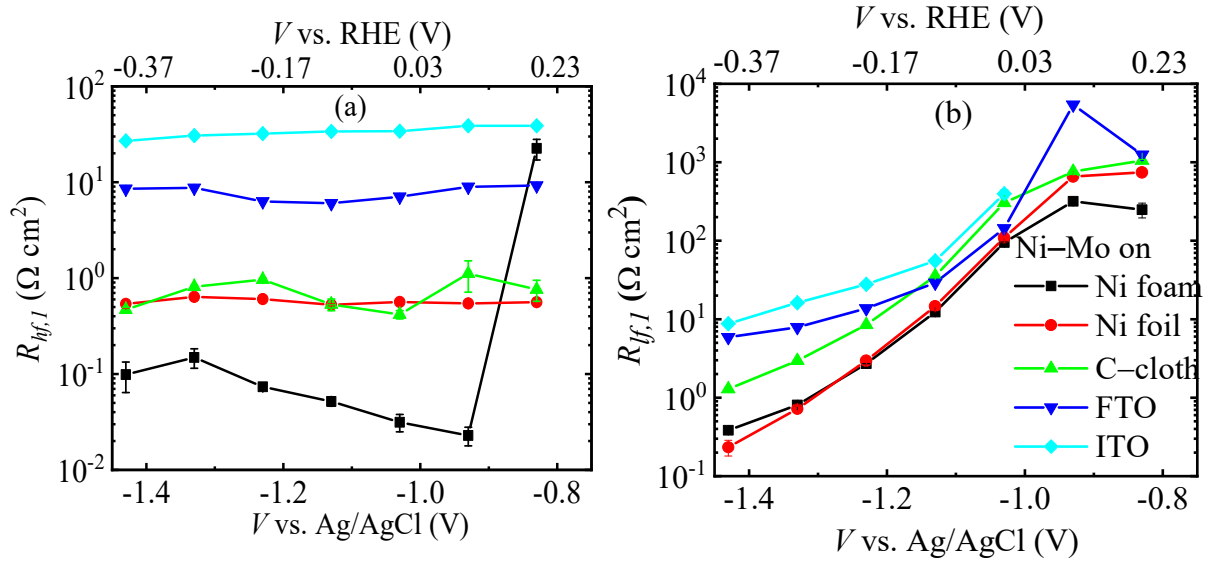
Figure 6. High–frequency (a) and low–frequency (b) resistance elements (R_{hf} and R_{lf}) from the fits of the *EqCrt1* model to experimental impedance data for Ni–Mo films on different substrates as a function of DC potential. Fits obtained using the model is shown as symbols connected with solid lines. Legends are shown in (b).

The potential dependence of the R_{lf} values for Ni–Mo films on different substrates obtained from the *EqCrt1* and *EqCrt2* models are shown in Fig. 6 (b) and S7 (b), respectively. The values of R_{lf} obtained from the two models were similar, at each potential. The dependence of the R_{lf} values on the substrates showed the same order as the substrate dependence of R_{hf} above the HER offset (at negative potentials). Thus, the R_{lf} values increased in the order of Ni foam, Ni foil, C–cloth, FTO and ITO. The R_{lf} values decreased with increased applied negative potential for Ni–Mo films on different substrates, which indicates that they should be associated with the reaction.

From the investigation of the DC potential dependence, one could note that R_s did not show significant changes at different DC potentials and was 1.28 Ω cm^2 in the *EqCrt1* model for the Ni–Mo films on Ni foam. However, it was highest for films on the high resistance substrates FTO and ITO. This indicates that R_s is not purely an electrolyte resistance but also includes a component

from charge transport through the substrate and the Ni–Mo film. The values of the sheet resistances (R_{sheet}) of the substrates are given in Table 1.

Table 1. The values of R_{sheet} of the substrates measured on a 1 cm^2 square area. The short–circuit resistance of the connections was 66 mΩ.

Ni–Mo on	R_{sheet} (Ω/sq)
Ni foam	0.1
Ni foil	0.2
C–cloth	0.6
FTO	14
ITO	43

From the substrate dependence of the all resistance values, R_{sheet}, $R_{s,1}$, $R_{hf,1}$, and $R_{lf,1}$, it was seen that the lowest resistance values were for the film on Ni foam and they increased in the order of Ni foil, C–cloth, FTO and ITO. This relation was obtained for all resistance values obtained from modeling, except for a few points which were probably affected by uncertainties in the fitting.

The small potential dependence of the high–frequency resistances indicates that there was no, or at most a small, effect of the reaction kinetics present in the high frequency region. That would indicate that the high–frequency resistances cannot be identified with the reaction charge transfer resistance and hence the *EqCrt2* model cannot be interpreted in terms of the theory of the HER. The strong substrate dependence of this parameter strongly suggests that it is due to a resistive interlayer, possibly at the substrate–film interface. The resistance $R_{lf,1}$ had strong potential dependence and increased in the order of Ni foam, Ni foil, C–cloth, FTO and ITO in the HER region at –300 mV vs. RHE. This is the same order as the current density in Fig. 3, which is expected in the case of the reaction charge transfer resistance. In the HER region $R_{lf,1}$ rapidly decreases with increasing negative potential, clearly signifying a strongly increasing HER reaction. The reaction resistance at positive potentials probably comes from parasitic side reactions. Hence

the low– and high–frequency semicircular arcs in the complex impedance plot appear to have different physical origins, which means that *EqCrt1* is a more physically realistic model for our samples.

The *T* parameter of the constant phase element in the high–frequency region, *CPE$_{hf}$–T*, and in the low–frequency region, *CPE$_{lf}$–T*, from fitting of the data of Ni–Mo films on different substrates to the *EqCrt1* and *EqCrt2* is shown in Fig. S9 (a, b) and S10 (a, b), respectively. The constant phase element exponent in the high frequency, *CPE$_{hf}$–P*, and in the low–frequency range, *CPE$_{lf}$–P*, obtained from *EqCrt1* and *EqCrt2* is shown in Fig. S11 (a, b) and S12 (a, b), respectively. The values of these parameters for each potential showed no clear dependence on applied potential and not any trend with the substrate. In what follows we will discuss the values of the *EqCrt1* model, as this appears to be the most physically realistic model in our case, as discussed above. Hence the low frequency *CPE* must be identified with the electrochemical double layer at the surface, while the high frequency *CPE* seems related to the substrate and/or substrate–film interface. The high frequency behavior can be rationalized with a Schottky–type barrier while the physical origin need more detailed investigations and could be both a single or double Schottky–barrier in the substrate-catalyst heterojunction or an oxide/hydroxide interface material created at the boundary.

The *T* and *P* parameters were used to define effective capacitances *C$_{hf}$* and *C$_{lf}$* in the high– and low–frequency regions, respectively, using[44-45]

$$C_{hf} = T_{hf}^{1/P_{hf}} \left[R_s^{-1} + R_{hf}^{-1} \right]^{(P_{hf}-1)/P_{hf}} \tag{5}$$

$$C_{lf} = T_{lf}^{1/P_{lf}} \left[(R_s + R_{hf})^{-1} + R_{lf}^{-1} \right]^{(P_{lf}-1)/P_{lf}} \tag{6}$$
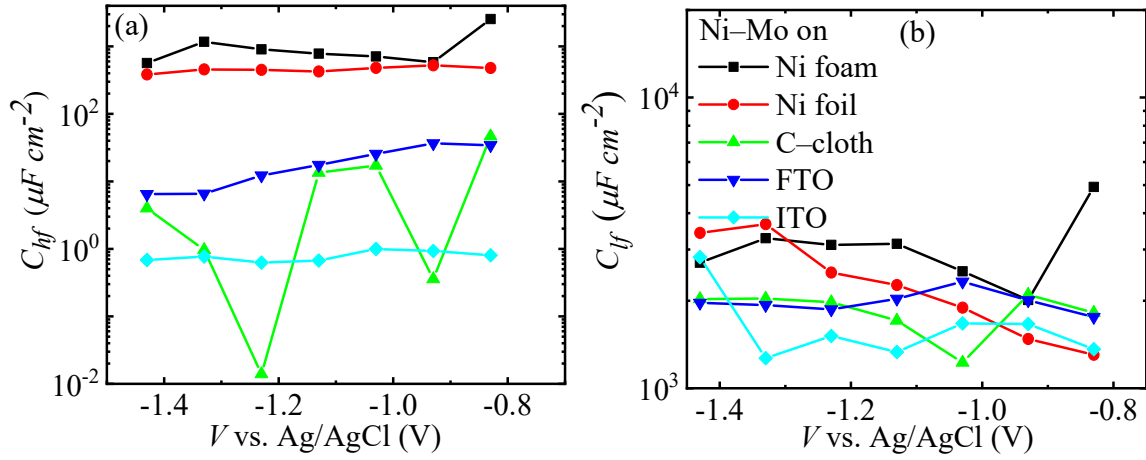
Figure 7. High–frequency (a) and low–frequency (b) effective capacitance (C_{hf} and C_{lf}) from the fits of the *EqCrt1* model to experimental impedance data for Ni–Mo films on different substrates as a function of DC potential. Legends are shown in (b).

The potential dependence of C_{hf} and C_{lf} is shown in Fig. 7 (a) and (b), respectively. It is observed that C_{lf} is larger than C_{hf}, which supports our identification of C_{lf} with the double–layer capacitance. The double layer should be thinner than any resistive interlayer film in the system and thus show a higher capacitance. C_{hf} showed a clear dependence on the substrate, which indicates that it is associated with the substrate–film interface. It was highest for Ni foam and decreased in the order of Ni foil, FTO, and ITO. This indicates that the interfacial barrier has a lower thickness for Ni foam and Ni foil than for the other substrates. The C_{hf} of C–cloth did not show any clear trend and was probably affected by large fitting uncertainties. The C_{lf} values did not differ significantly for the different substrates. Neither C_{hf} nor C_{lf} exhibited a significant potential dependence.

Table 2. The roughness factor r_f at 100 mV vs. RHE in low–frequency ranges estimated using C_{lf} calculated from *EqCrt1* model.

Ni–Mo on	r_f
Ni foam	101
Ni foil	74
C–cloth	105
FTO	100
ITO	83

Roughness factors (r_f) at 100 mV vs. RHE, in the non–HER region, were calculated from the ratio between the double–layer capacitance of the investigated electrodes and the capacitance value for a flat electrode (20 µF cm^{-2})[40] and are given in Table 2. The value of 20 mF cm^{-2} was chosen as a reference value obtained from a flat Pt electrode. The change in the double-layer capacitance can be used as measure of the accumulated double–layer capacity and is measured by the roughness factor. We obtain similar values of the roughness factor for both flat and porous substrates. The similarity of the r_f values is probably because the films on different substrates had the same geometric area. The Ni–Mo films were deposited by sputtering, which is a highly directional process. Hence, only surfaces of the porous substrates (Ni foam and C–cloth) that were facing the sputter target were probably coated.

4. Conclusions

In this paper, Ni–Mo alloys used as catalysts coated on Ni foam, Ni foil, C–cloth, FTO, and ITO substrates were examined. It was seen that the substrate had a significant effect on the HER. The lowest overpotential (–157 mV vs. RHE @ 10mA cm^{-2}) was obtained with the Ni–Mo film coated on the Ni foam; this was high compared to other alloy catalysts reported recently.[24, 25, 27] There was a correlation between the sheet resistance of the substrates and the overpotentials. EIS was

performed on Ni–Mo catalysts coated on different substrates in the HER and non–HER ranges. Two common equivalent circuit models were used for HER and the results showed that the data could be best explained using a so called double R–CPE model with a series connection of two parallel R–CPE circuits. The modeling showed that the series resistance depended on the sheet resistance of the substrate. The low–frequency resistance showed a systematic dependence on potential, which shows that it represents the reaction charge transfer resistance; therefore, the low–frequency constant phase element represents the double layer. The similarity of the roughness factors obtained from the double-layer capacitances for all substrates with different porosity can be explained by the directionality of the sputtering process. The high–frequency resistance was independent of the potential; therefore, it cannot be due to the HER. On the other hand, it was strongly dependent on the substrate resistance. This high–frequency response results may be interpreted as a Schottky–type barrier, which can be explained from either a heterojunction potential barrier or an oxide/hydroxide interlayer. The high-frequency resistance was lowest and the high-frequency capacitance was highest for Ni–Mo on Ni foam, indicating a less resistive and thinner barrier than for the other substrates. We conclude that the properties of this barrier strongly influence the overpotential and the efficiency of the HER.

Supporting Information

XRD patterns (Figure S1); SEM images and EDS elemental mapping (Figure S2); Nyquist plots (Figure S3-S5); equivalent circuit elements from the fits of the *EqCrt1* and *EqCrt2* models to experimental impedance data as a function of DC potential (Figure S6-S12).

References

(1) Guczi, L.; Erdőhelyi, A. *Catalysis for Alternative Energy Generation;* Springer, Springer Science Business Media, New York, 2012.

(2) J. Hildermeier, Electric vehicles in Europe – 2016 | Transport & Environment, Transp. Environ. 2016. https://www.transportenvironment.org/publications/electric-vehicles-europe-2016 (accessed 2019–02–25).

(3) Morrissey, P.; Weldon, P.; O'Mahony, M. Future Standard and Fast Charging Infrastructure Planning: An Analysis of Electric Vehicle Charging Behaviour. *Energy Policy*. **2016**, *89*, 257–270.

(4) Kyriakopoulos, G. L.; Arabatzis, G. Electrical Energy Storage Systems in Electricity Generation: Energy Policies, Innovative Technologies, and Regulatory Regimes. *Renew. Sustain. Energy Rev.* **2016**, *56*, 1044–1067.

(5) Zakeri, B.; Syri, S. Electrical Energy Storage Systems: A Comparative Life Cycle Cost Analysis. *Renew. Sustain. Energy Rev.* **2015**, *42*, 569–596.

(6) Palizban, O.; Kauhaniemi, K. Energy Storage Systems in Modern Grids—Matrix of Technologies and Applications. *J. Energy Storage*. **2016**, *6*, 248–259.

(7) Aneke, M.; Wang, M. Energy Storage Technologies and Real Life Applications – A State of the Art Review. *Appl. Energy.* **2016**, *179*, 350–377.

(8) Lavacchi, A.; Miller, H.; Vizza, F. *Nanotechnology in electrocatalysis for energy*; Springer, New York, 2013.

(9) Jacobsson, T. J.; Fjällström, V.; Sahlberg, M.; Edoff, M.; Edvinsson, T. A monolithic device for solar water splitting based on series interconnected thin film absorbers reaching over 10% solar-to-hydrogen efficiency. *Energy Environ. Sci*. **2013**, *6*, 3676–3683.

(10) Jacobsson, T. J.; Fjällström, V.; Edoff, M.; Edvinsson, T. Sustainable solar hydrogen production: from photoelectrochemical cells to PV-electrolyzers and back again. *Energy Environ. Sci*. **2014**, *7*, 2056-2070.

(11) Ardo, S. et al, Pathways to electrochemical solar-hydrogen technologies. *Energy Environ. Sci*. **2018**, *11*, 2768-2783.

(12) Bard, A. J.; Fox, M. A. Artificial Photosynthesis: Solar Splitting of Water to Hydrogen and Oxygen. *Acc. Chem. Res.* **1995**, *28*, 141–145.

(13) Chouhan, N.; Liu, R.–S.; Zhang, J. *Photochemical Water Splitting : Materials and Applications*; CRC Press, Taylor & Francis Group, Boca Ratón, 2017.

(14) Grätzel, M. Photoelectrochemical Cells. *Nature*. **2001**, *414*, 338–344.

(15) Navarro, R. M.; Alvarez–Galván, M. C.; Villoria de la Mano, J. A.; Al–Zahrani, S. M.; Fierro, J. L. G. A Framework for Visible–Light Water Splitting. *Energy Environ. Sci*. **2010**, *3*, 1865–1882.

(16) Walter, M. G.; Warren, E. L.; McKone, J. R.; Boettcher, S. W.; Mi, Q.; Santori, E. A.; Lewis, N. S. Solar Water Splitting Cells. *Chem. Rev*. **2010**, *110*, 6446–6473.

(17) Vilekar, S. A.; Fishtik, I.; Dattaz R. Kinetics of the Hydrogen Electrode Reaction *J. Electrochem. Soc.* **2010**, *157*, B1040–B1050.

(18) Lasia, A. *"Applications of the Electrochemical Impedance Spectroscopy to Hydrogen Adsorption, Evolution and Absorption into Metals", Modern Aspects of Electrochemistry*; Conway, B. E.; White, R. E. eds.; Kluwer/Plenum, New York, vol. 35, p. 1–49 (2002).

(19) Balbuena, P. B.; Subramanian, V. R., eds.; *Theory and Experiment in Electrocatalysis*; Springer New York, U.S.A., 2010.

(20) Zhao, G.; Rui, K.; Dou, X.S.; Sun, W. Heterostructures for Electrochemical Hydrogen Evolution Reaction: A Review, *Adv. Funct. Mater.* **2018**, *28*, 1803291.

(21) Sapountzi, F.M.; Gracia J.M.; Weststrate C.J. (K-J), Fredriksson O.A.H.; Niemantsverdriet, J.W. (H.) Electrocatalysts for the generation of hydrogen, oxygen and synthesis gas, *Progress in Energy and Combustion Science* **2017**, *58*, 1–35.

(22) Chen, Z.; Duan, X.; Wei, W.; Wang, S.; Ni, B-J. Recent advances in transition metal-based electrocatalysts for alkaline hydrogen evolution *J. Mater. Chem. A* **2019**, Advance Article.

(23) Strmcnik, D.; Lopes, P.P.; Genorio, B.; Stamenkovic, V.R.; Markovic, N.M. Design principles for hydrogen evolution reaction catalyst materials, *Nano Energy* **2016**, *29*, 29–36.

(24) Safizadeh, F.; Ghali, E.; Houlachi, G. Electrocatalysis developments for hydrogen evolution reaction in alkaline solutions – a review. *Int J Hydrogen Energy* **2015**, *40*, 256–74.

(25) McCrory, C. C. L.; Jung, S.; Ferrer, I.M.; Chatman, S.M.; Peters, J. C.; Jaramillo, T. F. Benchmarking Hydrogen Evolving Reaction and Oxygen Evolving Reaction Electrocatalysts for Solar Water Splitting Devices, *J. Am. Chem. Soc*. **2015**, *137*, 4347–4357.

(26) McKone, J. R.; Warren, E. L.; Bierman, M. J.; Boettcher, S. W.; Brunschwig, B. S.; Lewis, N. S.; Gray, H. B.; Evaluation of Pt, Ni, and Ni–Mo Electrocatalysts for Hydrogen Evolution on Crystalline Si Electrodes. *Energy Environ. Sci*. **2011**, *4*, 3573–3583.

(27) Zhang, L.; Xiong, K.; Nie, Y.; Wang, X.; Liao, J.; Wei, Z. Sputtering Nickel–Molybdenum Nanorods as an Excellent Hydrogen Evolution Reaction Catalyst. *J. Power Sources*. **2015**, *297*, 413–418.

(28) Qiu, Z.; Tai, C-W.; Niklasson G. A.; Edvinsson T. Direct observation of active catalyst surface phases and the effect of dynamic self-optimization in NiFe-layered double hydroxides for alkaline water splitting. *Energy Environ. Sci.* **2019**, *12*, 572–581.

(29) Bisquert, J. *Nanostructured Energy Devices : Foundations of Carrier Transport*; CRC Press, Boca Raton, FL, 2017.

(30) Barsoukov, E.; Macdonald, J. R. *Impedance Spectroscopy : Theory, Experiment, and Applications*; 2nd ed., John Wiley and Sons, New York, 2005.

(31) Lvovich, V.F. *Impedance Spectroscopy : Applications to Electrochemical and Dielectric Phenomena*, Wiley InterScience (Online service), Wiley, 2012.

(32) Harrington, D. A.; Conway, B. E. AC Impedance of Faradaic Reactions Involving Electrosorbed Intermediates – I. Kinetic Theory. *Electrochim. Acta*. **1987**, *32*, 1703–1712.

(33) Bai, L.; Harrington, D. A.; Conway, B. E. Behavior of Overpotential–Deposited Species in Faradaic Reactions–II. AC Impedance Measurements on H_2 Evolution Kinetics at Activated and Unactivated Pt Cathodes. *Electrochim. Acta*. **1987**, *32*, 1713–1731.

(34) Bard, A. J.; Faulkner, L. R. *Electrochemical Methods: Fundamentals and Applications*; 2nd ed.; John Wiley & Sons, Inc.: New York, 2001.

(35) Lasia, A.; Schlesinger, M. (Ed.) *Modeling of impedance of porous electrodes*, *Modern Aspects of Electrochemistry*, 43, Springer, 2009.

(36) Jakšić, J. M.; Vojnović, M. V.; Krstajić, N. V. Kinetic Analysis of Hydrogen Evolution at Ni–Mo Alloy Electrodes. *Electrochim. Acta*. **2000**, *45*, 4151–4158.

(37) Mayer, M.; Mayer, E. M. SIMNRA, A Simulation Program for the Analysis of NRA, RBS and ERDA, *AIP Conf. Proc.* **1999**, *475*, 541-544.

(38) Zview for Windows: Impedance/Gain Phase Graphing and Analysis Software–Operating Manual, Version 3, Scribner Associates, Southern Pines, NC, USA, 1996.

(39) Shinagawa, T.; Angel, T.; Garcia-Esparza, A. T.; Takanabe, K. Insight on Tafel slopes from a microkinetic analysis of aqueous electrocatalysis for energy conversion. *Sci. Rep*. **2015**, *5*, 13801.

(40) Losiewicz, B.; Budniok, A.; Rowinski, E.; Lagiewka, E.; Lasia, A. The Structure, Morphology and Electrochemical Impedance Study of the Hydrogen Evolution Reaction on the Modified Nickel Electrodes, *Intern. J. Hydrogen Energy*. **2004**, *29*, 145–157.

(41) Kubisztal J.; Budniok, A.; Lasia, A. Study of the Hydrogen Evolution Reaction on Nickel–Based Composite Coatings Containing Molybdenum Powder. *Int. J. Hydrogen Energy*. **2007**, *32*, 1211–1218.

(42) Sivula, K.; Le Formal, F.; Grätzel, M. Solar Water Splitting: Progress Using Hematite (α–Fe2O3) Photoelectrodes, *Chem. Sus. Chem*. **2011**, *4*, 432–449.

(43) Krstajić, N. V.; Jović, V. D.; Gajić–Krstajić, L.; Jović, B. M.; Antozzi, A, L.; Martelli, G. N. Electrodeposition of Ni–Mo Catalyst Coatings and Their Characterization as Cathodes for Hydrogen Evolution in Sodium Hydroxide Solution. *Int. J. Hydrogen Energy*. **2008**, *33*, 3676–3687.

(44) Brug, G. J.; van den Eeden, A. L. G.; Sluyters–Rehbach, M.; Sluyters, J. H. The Analysis of Electrode Impedances Complicated by the Presence of a Constant Phase Element. *Electroanal. Chem*. **1984**, *176*, 275–295.

(45) Hirschorn, B.; Orazema, M.E.; Tribollet, B.; Vivier, V.; Frateur, I.; Musiani, M. Determination of effective capacitance and film thickness from constant-phase-element parameters. *Electrochim. Acta* **2010**, *55*, 6218–6227.